# Drying of water from porous structures investigated by time-resolved X-ray tomography



**Author(s):**
Novák, Vladimír; Blažek, Miroslav; Schlepütz, Christian M.; Kočí, Petr; Stampanoni, Marco

**Publication date:**
2022

**Permanent link:**
https://doi.org/10.3929/ethz-b-000553190



**Originally published in:**
Drying Technology 40(16), https://doi.org/10.1080/07373937.2022.2076239

DRYING TECHNOLOGY
2022, VOL. 40, NO. 16, 3675–3693
https://doi.org/10.1080/07373937.2022.2076239



# Drying of water from porous structures investigated by time-resolved X-ray tomography

Vladimír Novák[a], Miroslav Blažek[b], Christian M. Schlepütz[a], Petr Kočí[b], and Marco Stampanoni[a,c]

[a]Swiss Light Source, Paul Scherrer Institute, Villigen, Switzerland; [b]Department of Chemical Engineering, University of Chemistry and Technology, Prague, Prague, Czech Republic; [c]Institute for Biomedical Engineering, ETH Zürich, Zürich, Switzerland

**ABSTRACT**

In this contribution, we apply time-resolved X-ray tomography to study drying of water in porous ceramic substrates used in emission control technologies. A time resolution of 2 s is achieved, and allows to observe the spatiotemporal distribution of water in structured porous materials. An image processing framework based on machine learning is introduced to track pore emptying and filling in a large number of 3D scans. Drying curves are extracted from the tomographic data to investigate drying in materials with different structural properties. Water redistribution by capillary pumping and rapid pore emptying by Haines jumps are observed, and their impact on drying dynamics is discussed. The relationship between the evolution of water clusters and different drying regimes is established. The obtained information on the interplay between pore emptying, water redistribution and the size of water clusters provides an important link between the structural properties of dried materials and their drying rate.

**ARTICLE HISTORY**
Received 6 January 2022
Revised 21 April 2022
Accepted 8 May 2022

**KEYWORDS**
Drying; time-resolved X-ray tomography; porous structure; Haines jump

## Introduction

Drying is a common unit operation used to control material properties in many industrial applications, including food, pharmacy, catalysis, ceramics, wood, building materials and sludge processing.[1] However, drying is an energetically highly intensive process, which amounts to 10–25% of the total industrial energy usage in most developed countries.[2,3] Environmentally-friendly drying technologies are being developed to reduce energy demand in order to address the challenges related to climate change, limited amounts of natural resources to produce energy, and the steep increase in energy consumption particularly in developing countries.[4] An optimal drying technology aims to deliver a high-quality product with a minimal energy input.

A prime illustration of the importance and impact of the drying process can be found in the field of heterogeneous catalysis, where reactor structuring from nanometers to millimeters represents an elegant pathway to process intensification.[5] A well-known example is a catalytic monolith reactor for air pollution control from mobile and stationary sources.[6] During the manufacturing process of a catalytic reactor, liquid is often removed from the porous structure by drying. Industrially established operations include deposition of active nanoparticles into a high surface area solid framework[7] and coating of an active material on porous substrates such as monoliths and foams.[8,9] Conditions applied during the subsequent drying step influence the quality of the final product and thus its functionality.[10–12]

Two different stages of drying with a distinct time-dependency of the drying rate are commonly observed.[13] In the first stage, the evaporation rate per unit area of the drying surface is independent of time. Hence, the regime is termed the *constant rate period* (CRP). The CRP is maintained as long as the liquid is wetting the outer surface of the material and the liquid vapor is being constantly removed. In the second stage of drying, the so-called *falling rate period* (FRP), the liquid meniscus recedes deeper into the pores of the material. The rate of evaporation decreases over time and the surface temperature rises

CONTACT Vladimír Novák vladimir.novak@psi.ch Paul Scherrer Institute, Forschungsstrasse 111, 5232 Villigen PSI, Switzerland.
Supplemental data for this article can be accessed online at https://doi.org/10.1080/07373937.2022.2076239

above the wet bulb temperature. As the meniscus is driven into the pores, the capillary flow of liquid to the outer surface slows down and the liquid is removed only by diffusion of its vapor. Both stages of drying are controlled by the structural properties of the material to drive the liquid or vapor toward the external surface. Behind this seemingly simple description of drying, a multi-phase, multi-scale and multi-physics problem is hidden. Extensive work has been carried out to understand heat transport processes between solid, liquid and gas phases occurring at multiple spatial and temporal scales.[4,14,15] The aim of such efforts is to predict drying rates from the knowledge of structural properties of the material to be dried, including pore size and shape, pore connectivity and contact angle.[16–20]

The development of predictive modeling tools to capture the structure-drying relationship requires access to experimental information about the processes, which occur inside a complex pore structure. Direct observation of water removal in 4D (space and time) provides an invaluable insight into the mechanism of drying. Several imaging techniques, including nuclear magnetic resonance, neutron and X-ray tomography, have been applied to observe drying nondestructively in porous structures. Magnetic resonance imaging (MRI) provides a spatially resolved measurement of moisture content.[21,22] However, the currently achievable spatial resolution of MRI (typically hundreds of μm) does not allow to observe moisture in individual μm-sized pores.[23] This is an important requirement, as many industrially relevant materials contain pores in micrometre size range.[24–26] Neutrons are very sensitive to hydrogen, which makes neutron imaging an interesting tool to investigate water distribution in porous materials. Also, neutron imaging achieves a higher spatial resolution of up to 15 μm/pixel compared to MRI.[27] Neutron radiography (2D images) was successfully used to investigate drying in real time.[28,29] However, neutron tomography is not practical to investigate water drying due to its long data acquisition times and consequentially low temporal resolution on the order of hours.[30] Laboratory-based X-ray tomography (XRT) was used to investigate the water distribution in drying-related applications.[31,32] Classical XRT is based on X-ray attenuation contrast, which was demonstrated to image water in large cavities and pores on the scale of hundreds of μm.[33] However, resolving pure water confined in μm-sized pores of a solid structure is challenging due to its small X-ray attenuation coefficient,[34] and currently beyond the capabilities of laboratory-based XRT. To overcome this limitation, contrast agents in the form of soluble salts, CaI or KI, can be added to the water to increase water contrast in such small pores.[35] Prior to using these additives, their impact on water properties, including surface tension, density and viscosity, should be considered. In addition, undesirable precipitation of the salt during drying should be also taken into account.

Imaging of pure water in μm-sized pores has become possible with the availability of partially coherent beams at synchrotron sources and the development of X-ray phase contrast imaging.[34] Information about the refractive index of a material can be obtained in addition to its attenuation coefficient, which can be used to enhance the contrast of weakly absorbing phases.[36,37] The phase contrast modality takes the advantage of stronger refractive effect compared to attenuation.[38] Furthermore, the high intensity of synchrotron radiation enables tomographic scanning with high acquisition speeds. Synchrotron-based X-ray tomography is thus currently the only imaging technique capable of capturing the dynamic evolution of multiphase systems with micrometre-scale spatial and second-scale temporal resolutions.[39,40]

In this contribution, we apply time-resolved X-ray tomography to observe the drying of water in porous cordierite, silicon carbide and aluminum titanate monoliths used in emission control technologies. The monoliths consist of parallel channels separated by porous walls. They are commonly manufactured with a variety of structural and material properties to meet the required functionality in different mobile and stationary applications.[41] The main aims of this contribution are (i) to demonstrate that a direct observation of water drying in complex structures by XRT is experimentally achievable, (ii) to develop an image processing framework based on machine learning to track pore emptying and filling in a large number of 3D scans, (iii) to extract drying curves from the tomographic data, and (iv) to discuss similarities and differences of the drying process in the studied materials, including water redistribution by capillary pumping, rapid pore emptying by Haines jumps, and the evolution of water clusters. The purpose of this work is to enable a direct investigation of the relationship between structural properties of a medium and its drying rate via 4D (space and time) imaging.

## Materials and methods

Drying of water was studied in three ceramic samples with monolithic channel structures and porous walls.

**Table 1.** Structural properties of ceramic monoliths. Average pore size and porosity were obtained by mercury intrusion porosimetry (MIP) and X-ray tomography (XRT).

| | | | | Average pore size ($\propto\mu$) | | Porosity (%) | |
|---|---|---|---|---|---|---|---|
| Sample | Channel density (cpsi) | Wall thickness (μm) | Channel size (mm) | MIP | XRT | MIP | XRT |
| Cordierite | 300 | 210 | 1.25 | 20.4 | 24.8 | 63 | 59 |
| Silicon carbide (SiC) | 260 | 315 | 1.30 and 0.9 | 18.7 | 21.5 | 56 | 52 |
| Aluminium titanate (AT) | 360 | 280 | 1.40 and 0.8 | 17.8 | 20.5 | 58 | 50 |

Asymmetric structures consist of two different channel sizes compared to the symmetric monolith whose channels are all of the same size, Figure 4.

The samples are labeled according to the material they are made of: cordierite ($Mg_2Al_4Si_5O_{18}$) as *cordierite*, silicon carbide (SiC) as *SiC* and aluminum titanate ($Al_2TiO_5$) as *AT*. The geometrical and structural properties of the samples are summarized in Table 1. The ceramic samples differ in the size of their monolith channels and the wall thickness. Cordierite exhibits a symmetric channel geometry (a single channel size), while SiC and AT represent asymmetric geometries (two different channel sizes). The structural properties, such as average pore size and porosity, were evaluated from mercury intrusion porosimetry (MIP) and X-ray tomography (XRT). A relatively small variation of average pore size and porosity was found between the samples.

Prior to the XRT study of the drying process, cross-section scanning electron microscopy (SEM) was used to obtain high resolution 2D images of the ceramic structures. Sections of each sample were cut out, mounted in epoxy resin and polished using diamond foils and colloid silica. The surface was then sputtered with a several nanometer thin layer of gold to prevent local charging. The specimens were scanned using a Tescan VEGA 3 SBU microscope and the backscattered electron (BSE) signal was used to achieve a higher contrast of the phases.

The samples were further characterized by mercury intrusion porosimetry using a Quantachrome PoreMaster 33 device. Approximately 1–2 $cm^3$ of the sample was placed in a measurement cell, degassed and filled with mercury. Subsequently, the pressure inside the cell was increased step-wise from 3 to 60,000 psi (ca. 20 kPa to 414 MPa) and the mercury intruded the pores of the sample. Pore diameters were calculated from the applied pressure by Washburn equation. Using this method, the porosity and pore-size distribution in the range of 3 nm–100 $\mu$m were determined.

Drying of water from the ceramic samples was investigated in 4D (time & space) by synchrotron-based X-ray tomography at the TOMCAT beamline (Swiss Light Source). A cylindrical segment, 12 mm in diameter and 20 mm in length, was cored from the monolith structure and wrapped in Teflon film. Subsequently, the sample was fixed into an aluminum holder mounted on a rotating stage, Figure 1. Prior to the drying experiment, the sample was filled with deionized water using a plastic pipette and the sample rotation was initiated at 180 degrees/s. Then two air heaters with a diameter of 25 mm (LE MINI from Leister) set to a constant temperature of 90 °C were moved into position at opposite sides of the sample. The rotating sample was thus heated simultaneously from two sides at the center of the monolith section.

Polychromatic X-ray radiation originating from a 2.9 T bending magnet source was used for all experiments. A 5 mm block of glassy carbon plus a 1 mm thick single crystal silicon wafer were inserted into the beam to filter out X-rays with low energies to decrease the heat load on the sample, resulting in an X-ray spectrum with a peak energy of about 26 keV. The in-house developed GigaFRoST camera[42] was used in combination with a high-resolution white-beam microscope (Optique Peter) with 13.7x magnification, yielding an effective pixel size of 0.82 μm. To capture the full extent of at least one or even several channels, an extended field-of-view scanning procedure was employed, where the rotation axis of the sample was aligned with one side of the detector's field-of-view and the sample was rotated through 360 degrees instead of the 180 degrees normally required for the parallel beam geometry.[43] The resulting field of view was $3951 \times 2016$ pixels, meaning that the size of the scanned section was $3160 \times 3160 \times 1653$ $\mu m^3$. The exposure time per projection was 1 ms with 2000 projections per 360° scan. Consequently, the total time to acquire a single scan was 2 s, and subsequent scans were acquired every 10 s to reduce the amount of the collected time-series data. During the 8 s pause between two scans, a fast X-ray shutter was closed to prevent unnecessary sample exposure to the beam. In total, between 110 and 130 scans were recorded per experiment, capturing approximately 20 min of the drying process.

The drying process of each sample was scanned twice: once without and once with a thermocouple. In the latter case, a 0.5 mm thick thermocouple was inserted into a central channel of the monolith sample

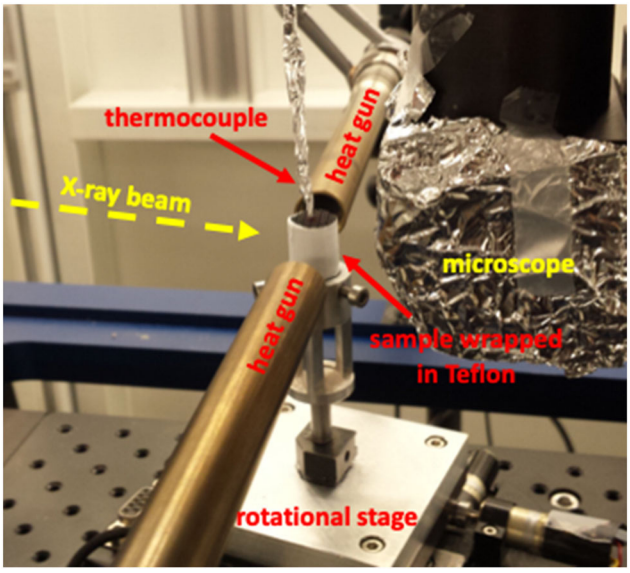


**Figure 1.** Configuration of the drying setup at the TOMCAT beamline including sample and sample holder, heat guns, thermocouple and microscope covered in aluminum foil to protect it from the heat.

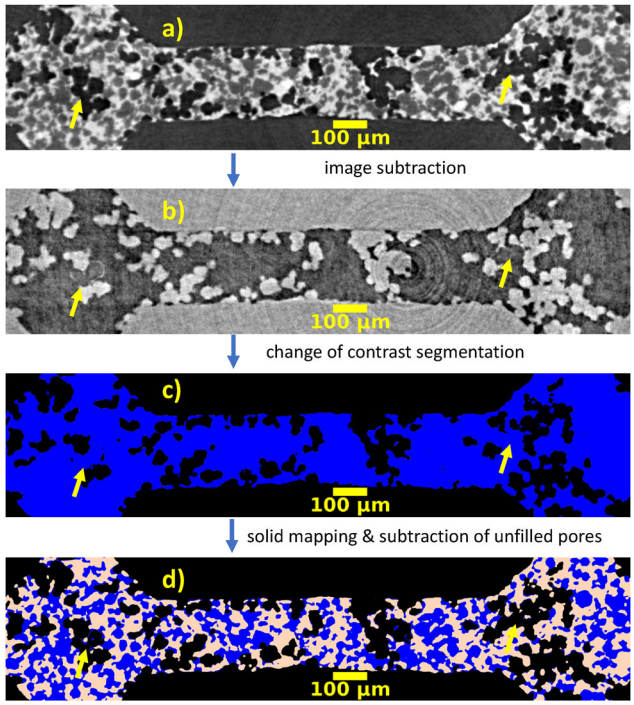


**Figure 2.** Segmentation process demonstrated on a section of the cordierite wall: (a) phase contrast reconstruction of a 3D image from X-ray projections collected at a given time *t*, solid ceramic is bright, air is dark and water intermediate gray; (b) subtraction of a reconstructed slice at time *t* from the reference slice at time $t = 0$ s (beginning of drying): bright gray stands for a contrast change due to water removal, dark gray means either pore filling by water or the unaltered state of the system with respect to the beginning of drying; (c) segmented contrast variation: bright gray from (b) becomes black and dark gray is assigned to blue; and (d) ceramic structure mapped over the segmented contrast variation to define pores of the ceramic wall: water (blue), air (black) and solid ceramic (salmon). Yellow arrows indicate pores which were not filled during soaking in water prior drying and thus no contrast change was observed during water removal. These pores were treated separately and subtracted from the segmented image, compare Figure 2b and d.

to measure the temperature evolution during water removal. A control experiment without X-ray beam showed that the filtered X-ray beam induced only a minor temperature rise of ca 2 °C. The temperature gradient measured across the sample diameter was also minimal, with the core perimeter being ca. 2 °C cooler than the center. The sample rotation was not centered in the X-ray beam nor in the hot gas stream originating from the heat guns due to the extended field-of-view scanning procedure. The rotation offset can thus slightly lower the temperature in the external channels. The temperature difference along the monolith channel was about 6 °C. However, somewhat lower temperatures were observed in the last few millimeters of the monolith sample, which was fixed in the aluminum holder, yielding, on average, a ca. 13 °C temperature difference.

The obtained 3D volume data sets from the time-resolved X-ray tomography scans were reconstructed using the propagation-based phase contrast method[44] and the gridrec algorithm.[45] Weakly absorbing water becomes visible in the grayscale reconstruction due to the retrieval of phase shift information caused by X-ray refraction, Figure 2a. For quantitative analysis of the drying process, the reconstructed images can be segmented by assigning a unique phase to each pixel of the grayscale map: air, water or solid ceramics. However, similar gray levels of water and air accompanied by a local contrast variation make standard thresholding methods inefficient. The challenge of multiphase segmentation is to capture correctly the transition between solid ceramics and air without being assigned falsely to a thin water film as demonstrated by Kohout, et al.[33] In addition, the large number of scans obtained during time-resolved scanning (over 100 per sample) demands an automatic and efficient image processing framework. This requirement is further emphasized by the fact that one drying experiment takes approximately 20 min; however, 3D reconstruction, image processing and segmentation of a terabyte-sized time series is significantly more time-consuming.

Here, we demonstrate a processing framework, which was developed and used to systematically analyze 3D images of the drying process collected by time-resolved X-ray tomography. A 3D image at a

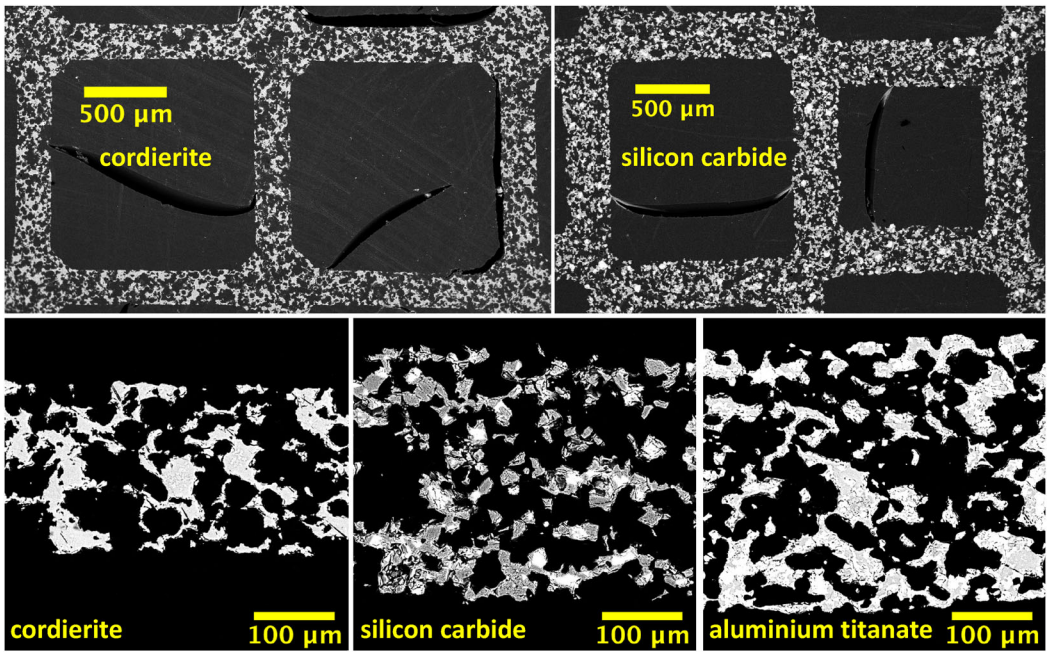


**Figure 3.** Images from cross-section scanning electron microscopy (SEM). Top row: cordierite with symmetric channels and silicon carbide with asymmetric channels. Bottom row: detail view of the ceramic wall structure for cordierite, silicon carbide and aluminum titanate.

given time $t$ was first subtracted from a 3D image at time $t = 0$ s to capture the contrast variation due to a change in water occupancy, Figure 2b. Prior to subtraction, the time series of 3D images were registered to ensure that the temporal changes of the contrast originate from the spatial variation in water distribution and not from the sample movement. The *3D correct drift*[46] and *StagReg*[47] plugins integrated in ImageJ/Fiji[48,49] were used for that purpose. In a subtracted image, an increase of contrast corresponds to water removal. On the other hand, a decrease of contrast indicates pore filling by water. In addition, no contrast variation represents an original state of the system after water saturation including pores and solid structure.

The 3D subtracted images were segmented using the Trainable Weka Segmentation package.[50] First, regions with bright and dark gray levels were selected manually in the center slice of the 3D stack for each sample to train the machine learning algorithm. It needs to be considered that water in monolith channels represents about 70–80% of all water in the studied samples. Due to this large volume, the water signal from the channels comes mostly from X-ray absorption. On the other hand, the phase shift is more sensitive to water confined in the micrometre sized pores due to low X-ray attenuation of such a small volume. Therefore, monolith channels and porous walls required different sets of training data. The training process thus generated two classifiers for each sample: (i) channel and (ii) wall. Training features chosen to obtain a visually accurate representation of the segmented image included Gaussian blur, edges, mean and variance in combination with fast random forest.

The classifiers were then used to assign a value of zero to the water-free space and a value of one to the space occupied with water or ceramic framework. To reduce the computational demands, a representative sub-stack of 400 slices was segmented out of the 2016 slices. Figure 6 and the related discussion show that the proposed stack reduction along the monolith channel does not affect the data interpretation. A binary mask separating the wall and channel space was subsequently used to combine the segmented time series obtained for the two classifiers, Figure 2c. The mask was generated by a closing operation performed on the segmented ceramic structure. Compared to air, the solid phase of the monolith structure is formed of heavier atoms such as Si, Al, Mg in cordierite, Si in silicon carbide or Al, Ti in aluminum titanate. This allowed to use a simple thresholding method on an un-subtracted 3D image at the end of drying, which contained no water. The segmented ceramic structure was then mapped to the segmented time series in Figure 2c to differentiate water regions from the solid phase, Figure 2d.

The described image processing assumes that all pores are filled with water prior to drying. Therefore, a contrast change can be assigned to either pore

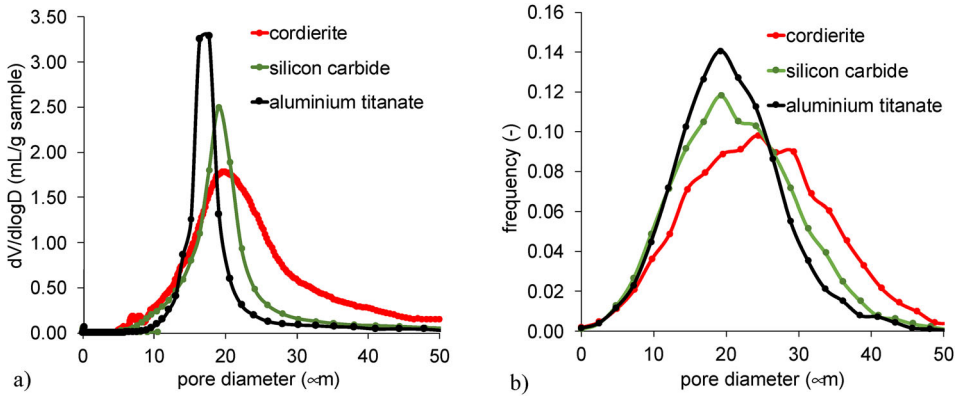


**Figure 4.** Pore size distribution of the ceramic monolithic structures obtained from (a) mercury intrusion porosimetry (pore neck diameter) and (b) X-ray tomography (geometrical size of the pore body).

emptying or pore filling. However, air can be trapped inside the ceramic structure during the soaking process. In an unfilled pore, no contrast variation can be observed during drying, as illustrated by comparison of the regions marked with yellow arrows in Figure 2a, b. Such pores thus appear constantly saturated even in a segmented dried porous structure. Comparison of subtracted and un-subtracted images at the end of drying allows to identify these unfilled pores and subtract them from the segmented 4D water profile, as shown by the yellow arrows in Figure 2d. In conclusion, the introduced processing step thus assigns unambiguously each pixel in the 4D images to solid, water or air, yielding a pore-scale profile of water evolving over time.

In the segmented time-series, the geometrical size of empty pores in the ceramic wall was obtained by using the *local thickness* plugin integrated in ImageJ/Fiji.[51] In addition, water clusters in each time step were identified and quantified by using the *3D object counter* in ImageJ/Fiji.[52]

## Results

Structural differences between the samples are revealed by scanning electron microscopy. Examples of symmetric and asymmetric channel geometries are shown in Figure 3 for cordierite and SiC, respectively. The high-resolution images in Figure 3c,d demonstrate the differences in pore shape and connectivity observed in the individual samples. Such a structural variability of the wall morphology is not captured by simple average quantities such as the porosity and average pore size shown in Table 1. Pores can be described by their geometrical size (based on the internal pore space) or by the neck size (determined by the largest available entrance to the pore body). Note that the mercury porosimetry curves in Figure 4a are sensitive to the size distribution of the pore necks, which separate individual pores inside the ceramic walls.[53] The aluminum titanate sample possesses the lowest mean pore neck size and the narrowest distribution, silicon carbide shows a somewhat larger mean size and wider distribution, while the largest pore necks with the broadest size distribution are observed in the cordierite sample. The pore size distribution obtained from XRT image analysis captures the geometrical size of the pore bodies inside the ceramic wall,[51] Figure 4b. The results confirm the largest pores and the broadest distribution in the cordierite sample. The sizes of pore bodies in the SiC and AT samples seem to be relatively similar, with SiC containing only slightly more larger pores. The main difference between SiC and AT thus remains in neck size distribution (Figure 4a), indicative of significantly narrower pore entrances in AT. Another aspect that must be considered is that even though cordierite contains, on average, the largest pores of all three samples, its wide size distribution means that it also contains a considerable amount of relatively small pores. Note that cordierite contains more pores with neck sizes below 15 microns than SiC (Figure 4a).

An example of changing water distribution during drying is shown for the silicon carbide (SiC) monolith in Figure 5a. The so-called drying curve depicts the temporal evolution of the water fraction obtained from the segmented 3D images. A water fraction of 100% signifies an initial state of the sample after soaking in water. The corresponding 2D snapshot at time $t = 0$ s demonstrates that the monolith channels and the majority of the porous walls were saturated with water. However, a few, predominantly larger, pores inside the wall were not filled during the soaking. Porosity analysis of all three samples indicates that less than 2.5% of the pore volume in the wall remained empty.

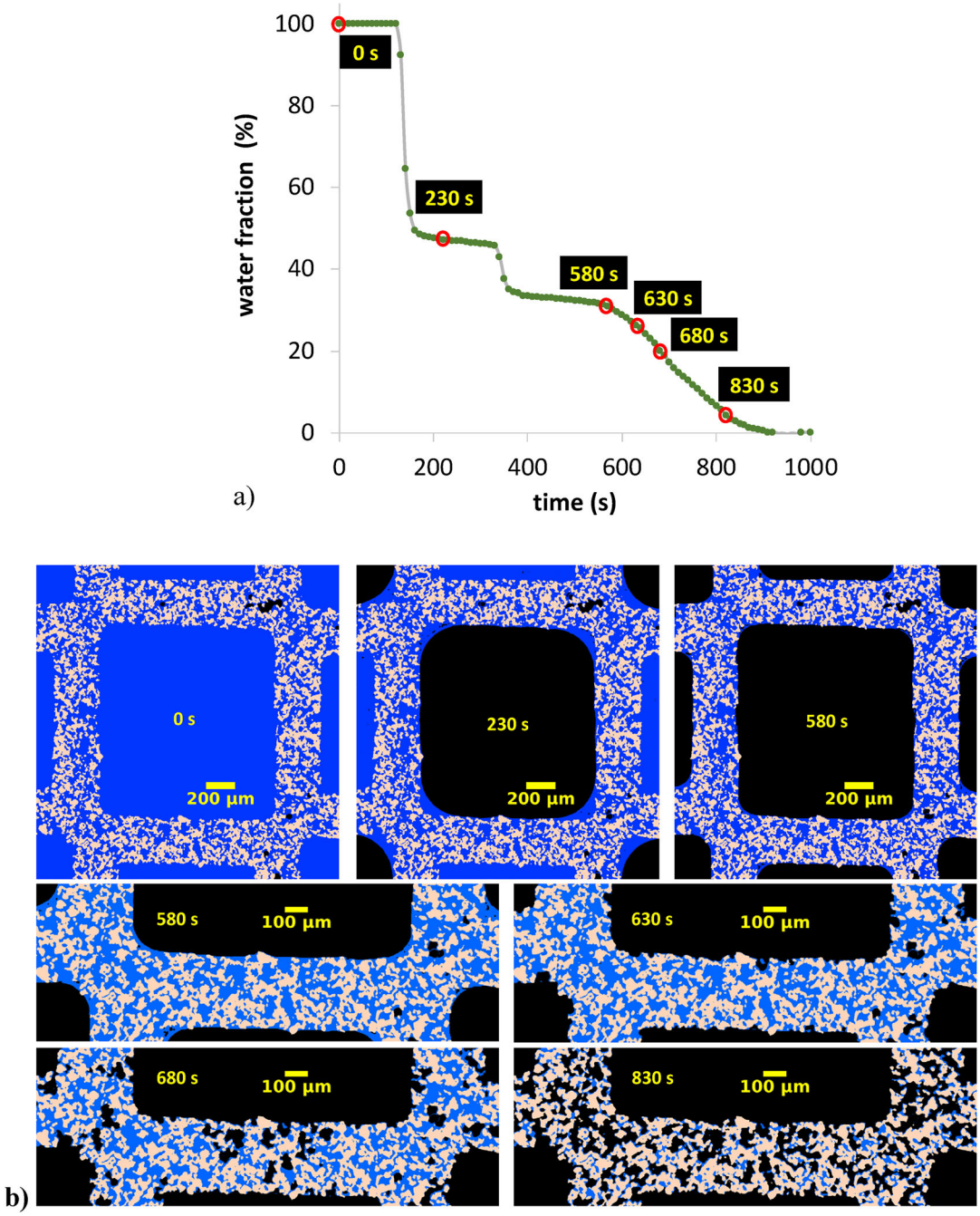


**Figure 5.** (a) Drying curve of silicon carbide with asymmetric channels capturing the evolution of the water fraction as a function of drying time. The initially soaked system corresponds to 100%. Red circles on the drying curve mark the time points of the accompanying structural snapshots below. (b) The snapshots with segmented air (black), water (blue) and ceramics (salmon) illustrate the water distribution in a monolith channel and in a section of the wall.

The drying curve of SiC reveals three pronounced steps, Figure 5a. The initial two steep decreases of the water volume fraction correspond to the bulk water removal from the scanned section of the monolith channels. Let's remember that the SiC monolith contains two different channel sizes. At first, the bigger channels were emptied at about $t = 120$ s, followed by the smaller channels at $t = 320$ s. Once the water meniscus retreated from the scanned section of the big channel, a water film formed in the corners. Closer inspection of the snapshot at $t = 230$ s revealed that a thin film covered the whole outer surface of the ceramic wall, Figure 5b. Similarly, the water film also formed in the corners of the small channels once the meniscus receded deeper into the monolith.

The moving meniscus was likewise captured in the resliced images along the monolith channel at $t = 130$ and $t = 340$ s for the larger and the smaller channel,

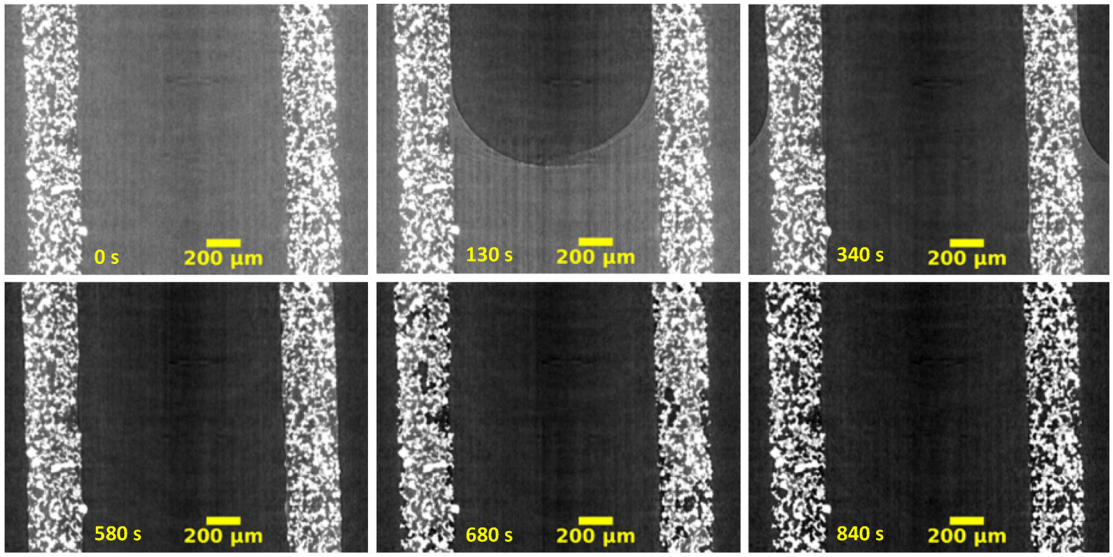


**Figure 6.** Drying series of the silicon carbide sample resliced along the monolith channel. The plane shown here cuts through the center of the asymmetric channel structure. The images depict the whole length of the scanned channel section with dimension $2.18 \times 1.64\,mm^2$. Dark pixels show air, mid-gray water, and bright ceramics. The corresponding video is available in the supporting information (Video S1). The other studied samples, cordierite and AT, are also shown for comparison in the supporting information (Videos S2 and S3, respectively).

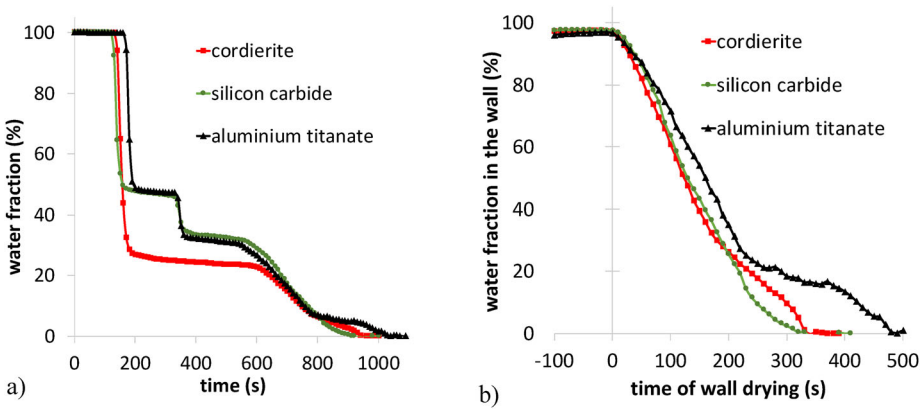


**Figure 7.** Drying curves for all studied ceramic monoliths. The evolution of the water fraction over time is obtained from the segmented images: (a) global water profile including monolith channels and ceramic walls; (b) water profile only inside the porous walls with $t' = 0$ s indicating the onset of wall drying.

respectively, Figure 6. The images are un-processed to demonstrate water distribution in the whole scanned section of the SiC sample. As the drying occurred on all water-air interfaces, including the corner film and the walls, it implies that bulk water was transported from the channels both along and across the wall (i.e., between the channels). Note that the pores inside the ceramic wall are about two orders of magnitude smaller than the monolith channels, Table 1, which indicates that capillarity is the driving force.[54]

When the bulk of the water had been removed from the channels, the corner film diminished, which was followed by drying of porous walls. The wall drying is indicated by a more gradual reduction of the water fraction on the drying curve starting at around $t = 580$ s, Figure 5a. The tomographic images indicate that air invaded the wall independently of the channel size, which was the consequence of water redistribution between the channels due to capillary forces, Figures 5b, 6 and Video S1. Drying of water from the monolith channels thus progresses in a hierarchical manner, starting in the large channels, followed by the small channels, and finally in the pores of the ceramic wall. Such a hierarchy can span from the millimeter to the nanometer scale, as recently demonstrated in our previous work for a ceramic monolith coated with micro/mesoporous materials.[23]

The drying curves of all studied samples are compared in Figure 7a. Similar to the case of SiC, the curve for aluminum titanate (AT) showed two initial

**Table 2.** Drying durations for cordierite, silicon carbide (SiC) and aluminum titanate (AT).

| Sample | Drying time (s) | | | Volume of wall water normalized to cordierite (-) | Wall drying time normalized to cordierite (s) | Relative wall drying time normalized to cordierite (%) |
|---|---|---|---|---|---|---|
| | Total | Channel | Wall | | | |
| Cordierite | 960 | 630 | 330 | 1.00 | 330 | 100 |
| Silicon carbide (SiC) | 910 | 600 | 310 | 1.34 | 232 | 70 |
| Aluminium titanate (AT) | 1040 | 550 | 490 | 1.15 | 427 | 129 |

*Drying time* indicates the time needed to remove the water from the whole sample (total), the channels, or the wall; *volume of wall water normalized to cordierite* measures the relative difference of the pore volume normalized to cordierite and *wall drying time normalized to cordierite* is the time that would be needed to remove a volume of water equivalent to the cordierite sample.

steep steps on the drying curve, which are attributed to the emptying of the two differently sized channels in the asymmetric channel structure. On the contrary, the cordierite sample with symmetric channels exhibited just a single initial step. The subsequent gradual decrease of the water fraction in the last stage of all three drying curves represents water removal from the ceramic wall. It is important to notice that air penetrated the porous wall in all samples only after the channels were completely dry, as described above for SiC. Water was thus redistributed throughout the structure, keeping the pores of the wall on the drying front saturated, cf. Videos S1–S6. Consistently, the onset of the wall drying did not depend on the location in the monolith channel.

The drying curves in Figure 7a also determine the length of drying, which is an important indicator of the energy consumption and economic costs of the drying process. Drying of the monolith channels took approximately 50% to 66% of the total drying time, Table 2. However, weak capillary forces inside the millimeter-sized channels typically allow to use energetically less demanding strategies, including air knife[8] and vacuum,[55] to remove water from the channels. Therefore, the wall drying time can be considered as a more relevant indicator of the drying cost and we will focus on this process from here on.

Figure 7b captures the corresponding evolution of water inside the ceramic walls. The onset of the wall drying was shifted to $t' = 0$ s and the water fraction plotted on the $y$-axis shows just the water confined in the porous wall and thus excludes water in the monolith channels. Considering this re-normalization of the $x$- and $y$-axes, the drying curves can be directly compared to reveal similarities and differences of water removal dynamics amongst the studied samples. The slope of the drying curve defines the drying rate of water inside the wall and its change indicates a transition from one drying mechanism to another. The drying rate is constant for each of the three samples in the first drying period (the linear segment up to $t \sim 200$ s in Figure 7b; the drying rates are: SiC 0.30 ml/m$^2$/s > cordierite 0.28 ml/m$^2$/s > AT 0.27 ml/m$^2$/s). However, much more pronounced differences were observed in the second drying period, indicated by the changing slope of the drying curve. Such a variation of the drying rate can be only attributed to the structural properties of the individual samples, such as pore size, shape and connectivity. The fastest wall drying, taking 310 s in total, was observed for SiC. On the other hand, AT showed the longest wall drying time of about 490 s. Note that these values do not consider differences in the pore volume of individual samples due to variations of the wall thickness and porosity, Table 1. Therefore, an extrapolated wall drying time, normalized to the cordierite pore volume, is also shown in Table 2. These normalized values indicate that the wall drying in SiC is about 30% faster than in cordierite. The slowest wall drying is still observed for AT, which takes about 29% and 59% longer than cordierite and SiC, respectively.

The impact of the pore structure on drying can be observed in the evolution of surface water on the ceramic wall as compared to bulk water inside the wall, Figure 8a. The surface water is defined here as water in the 4 µm (5 pixels) thick layer at the entrance into the ceramic structure. Bulk water is then located in the remaining space of the porous wall. Analysis of surface and bulk water provides information about the capillary flow from inside of the porous wall toward the channel-wall interface.[56] A sharp decrease of the surface water fraction is observed at the onset of the wall drying when water menisci developed at the wall-channel interface and subsequently retreated into the ceramic wall. This process coincides with a steep increase of the drying rate, which is commonly denoted as the *initial drying period*. The following plateau of the drying rate marks the *constant rate period* (1$^{st}$ CRP) with a linear decrease of water fraction over time. Note that the drying rate shown in Figure 8a is per m$^2$ of pore space rather than per m$^2$ of the entire porous material to allow direct comparison of the samples possessing different porosity. With the start of the 1$^{st}$ CRP, the initially rapid decrease of surface water slowed down and subsequently followed a linear trend of a gradual decrease in time as some

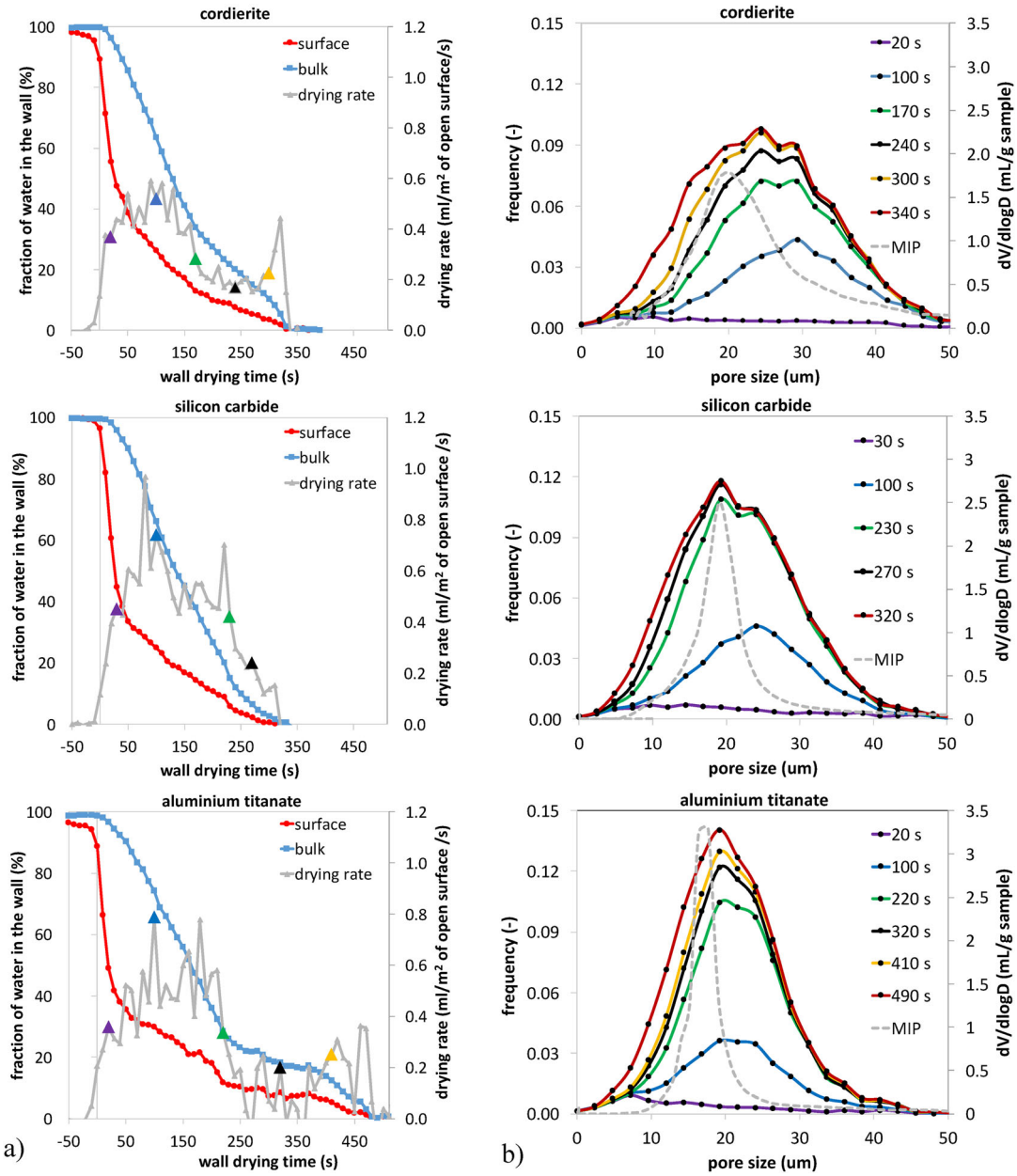


**Figure 8.** (a) Evolution of the surface water fraction in a 4 μm (5 pixels) thick layer at the channel-wall interface, the bulk water fraction in the remaining volume of the ceramic wall, and the wall drying rate, plotted for all three samples. (b) Size distribution of empty pores (containing no water) for selected time steps. The color of the size distributions corresponds to the colored triangles on the drying rate curves in Figure 8a. The gray dashed size distribution of pore necks is obtained from mercury intrusion porosimetry (MIP) of empty ceramic samples.

menisci from the channel-wall interface retracted into the wall. Drying of water from such external surfaces is typically faster than drying of bulk water confined in a pore structure, as it is not limited by diffusion of its vapors.[13] However, surface and bulk water show a correlated linear decrease, which indicates that water is transported from the interior of the porous wall toward the channel-wall interface, where it is subsequently evaporated. The number of empty pores naturally increased as water was removed from the ceramic structures. Figure 8b shows the size distribution of empty pores for the selected time steps. Interestingly, larger pores were preferentially emptied at the beginning and then followed by the smaller ones later on in all three samples. As drying occurred on all water-air interfaces, the obtained distributions point toward water redistribution from large to small pores taking place in addition to water transport from inside the wall to its external surface. The end of the 1st CRP is manifested by a decrease of the drying rate, occurring around the time step marked with the green triangle in Figure 8a.

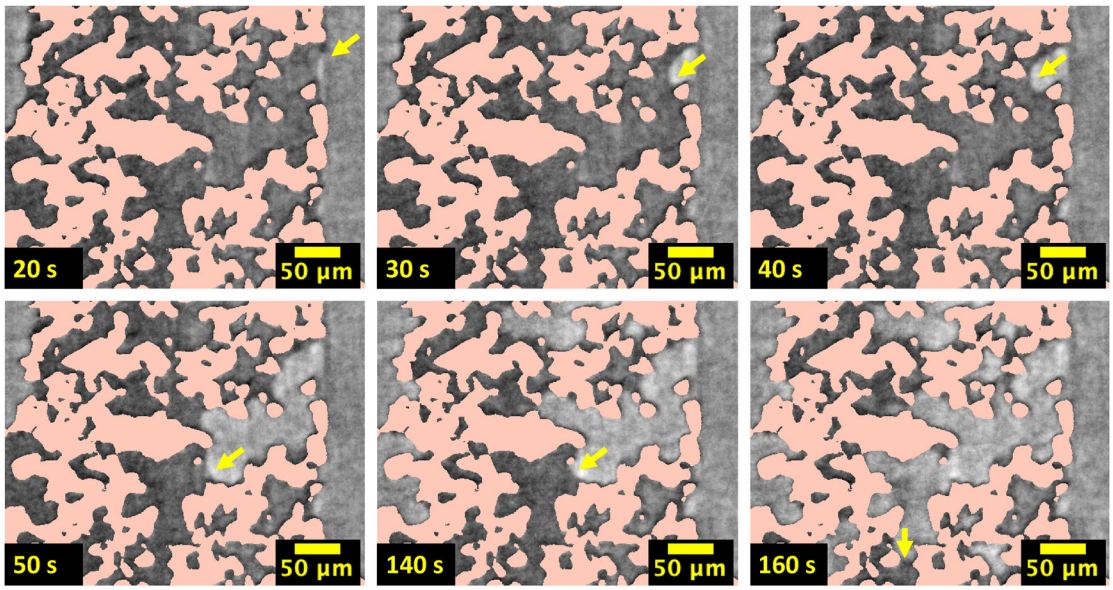


**Figure 9.** Meniscus formation and pore emptying captured on a series of snapshots in the silicon carbide sample. The images are 2D slices obtained from subtracted 3D tomograms: dark gray denotes water; bright gray corresponds to emptied pores and the solid material is mapped in salmon color. The yellow arrows indicate the cascade of events, which took place during emptying of the wall pores. The time indicated in the bottom left corner of each snapshot refers to wall drying time $t'$.

Detailed snapshots of drying reveal the mechanism of water redistribution in the silicon carbide (SiC) sample, Figure 9. At the wall drying time $t' = 20$ s, a meniscus was formed at the pore entrance into the solid structure, indicated by the yellow arrow. Subsequently, the meniscus receded into the wall until a constriction (pore neck) was reached at $t' = 40$ s. As the water-air interface moved behind the pore neck into a pore opening, the capillary pressure $p_c$ suddenly dropped due to the decrease of the meniscus curvature $2/r$ as shown by the Young-Laplace equation:

$$p_c = \frac{2\gamma\cos\theta}{r} \quad (1)$$

where $\gamma$ is the surface tension, $\theta$ the wetting angle and $r$ the pore radius. Such a capillary instability caused an abrupt emptying of the larger pore behind a constriction, which is known as a Haines jump.[57] Stable menisci were subsequently formed in the pore necks of similar or smaller sizes. The rapid emptying of a pore body allowed to equilibrate the capillary pressure in the interconnected system of many saturated pores, as seen for the time point at $t' = 50$ s in Figure 9. The drying front thus moved deeper into the ceramic wall. The curvature of the newly formed meniscus increased with time, however its location remained stable for 90 s until another Haines jump took place at $t' = 140$ s. Since evaporation kept occurring on every water-air interface in the interim, water had to flow through the interconnected pore system toward the studied meniscus to maintain its position. Therefore, capillary pressure drives the water redistribution between the stable menisci in different pores by capillary flow. Similar conclusions are made for cordierite and aluminum titanate structures, refer to the Videos S7–S9 in the supporting information.

The drying dynamics of the ceramic wall thus resembles a cascade of events, where states with a relatively stable meniscus configuration (stationary or relatively slowly receding) are interjected by rapid pore emptying (Haines jump) events. The capillary instability causing a Haines jump is controlled by the size of the pore neck, which defines a pressure when the pore empties.[58] Let us remember that the size of the pore necks can be obtained from mercury intrusion porosimetry (MIP),[53] Figure 4a. Mercury does not wet the surface of the ceramic structure and thus a higher pressure has to be applied to fill a smaller pore. In case that a smaller pore neck restricts access to a larger pore body, the latter is spontaneously filled only once the pressure is high enough to push the mercury through this constriction. Figure 8b shows neck size distributions compared to the temporal evolution of empty pores.

During the 1st CRP, water in the SiC sample is removed from predominantly larger pores by Haines jumps. The end of the 1st CRP coincides with the emptying of 97% of those pores bigger than the average neck size, green curve in Figure 8b. This indicates that when the water redistribution via Haines jumps is reduced, the drying rate decreases, see green triangle in Figure 8a. In case of cordierite and aluminum

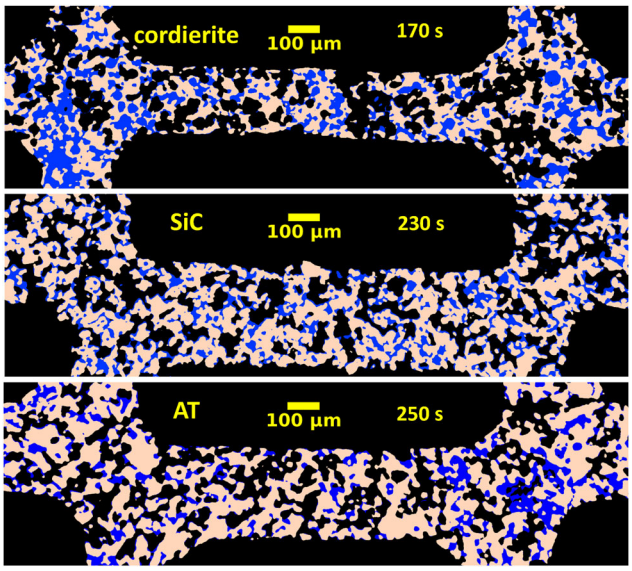


**Figure 10.** Snapshots of water distribution inside the ceramic wall of cordierite, silicon carbide (SiC) and aluminum titanate (AT) at the end of the first constant rate period (1st CRP). Blue color denotes water, black corresponds to air, and the solid material is mapped in salmon color. The wall drying time indicated in each sub-figure indicates the end of the 1st CRP, which corresponds to the green color and triangle in Figure 8.

titanate (AT), a somewhat smaller number of pores larger than the average neck size was emptied by the end of the 1st CRP (88% and 90%, respectively). Temporal snapshots at the end of the 1st CRP revealed that water is uniformly distributed across the ceramic wall and particularly in the smaller pores in the SiC sample, while cordierite and AT showed an inhomogeneous water distribution with some large pores still completely filled with water, see Figure 10. Focusing on the structural differences between SiC and the other two samples, we notice in Figure 8b that the mode pore neck size in the empty SiC substrate (determined from MIP) coincides with the mode pore size (determined from XRT). However, cordierite and AT samples show a larger mode pore size than their mode pore neck size. This indicates a higher probability of large pores being "locked" behind narrow pore necks in cordierite and AT, which agrees with the observation in Figure 10.

The subsequent transition from the 1st CRP to a slower drying regime can be better understood by an analysis of water clusters inside the ceramic walls. The temporal evolution of large water clusters was analyzed in the segmented 3D images, Figure 11. Large clusters are defined here as having at least 150 times the volume of the average geometrical pore size determined by XRT, Table 1. A large cluster thus represents a body of water which spans over a network of interconnected pores, where Haines jumps can presumably occur. At the beginning of drying, one large water cluster occupies the whole ceramic wall. This large cluster subsequently shrinks as water is removed from the wall during the 1st CRP, see yellow diamonds in Figure 11. Most of the water body remained interconnected in this primary large cluster in all three samples. It is only toward the end of the 1st CRP, that the water fraction in the large cluster deviates from the total water fraction on the drying curve as the water domain breaks into smaller clusters. Some of the new clusters are still large enough to be classified as large clusters according to the definition used here and thus are shown as additional yellow diamonds in Figure 11. Concurrently, the volume of water contained in the smaller clusters grows, which is accompanied by an increase of the total number of clusters. Disintegration of the large cluster disconnects bulk water from the surface, which restricts the transport pathways to the external surface. Water evaporation in confined pores is known to be a slower drying mechanism compared to evaporation from external surfaces, as it is limited by diffusion of its vapor.[13] The disintegration of the large cluster thus explains the decrease of the drying rate after the end of the 1st CRP.

The disintegration of the primary large cluster alone does not explain the occurrence of the 2nd CRP in the cordierite and AT samples, Figure 7b. Therefore, also the temporal evolution of smaller clusters was evaluated from the segmented 3D images, Figure 11. The small clusters included in the analysis have a minimal volume equivalent to a sphere with a diameter of 4 µm (5 pixels), which is the minimum size required for the accurate spatial resolution of a cluster. The number of clusters was increasing from the onset of drying and this process accelerated particularly around the first transition. In an open system, where the rate of evaporation is the limiting step, the amount of water removed as a function of time is directly proportional to the water-air surface area. As clusters continue to split and the evaporation surface increases, the amount of water dried over time should also increase. However, the linear decrease of the water fraction observed in the 2nd CRP of the cordierite and AT samples (Figure 11a,c) indicates a constant drying rate. This suggests that vapor transport through the ceramic wall limited the drying rate. Toward the end of the 2nd CRP, the number of clusters in the cordierite and AT samples reached its maximum. After that point, more cluster were disappearing than being generated and the decline of the number of clusters correlates with the end of the 2nd CRP. In contrast, the disintegration of water clusters in the SiC wall (Figure 11b) was faster in comparison with cordierite and AT. The maximum number of clusters was reached

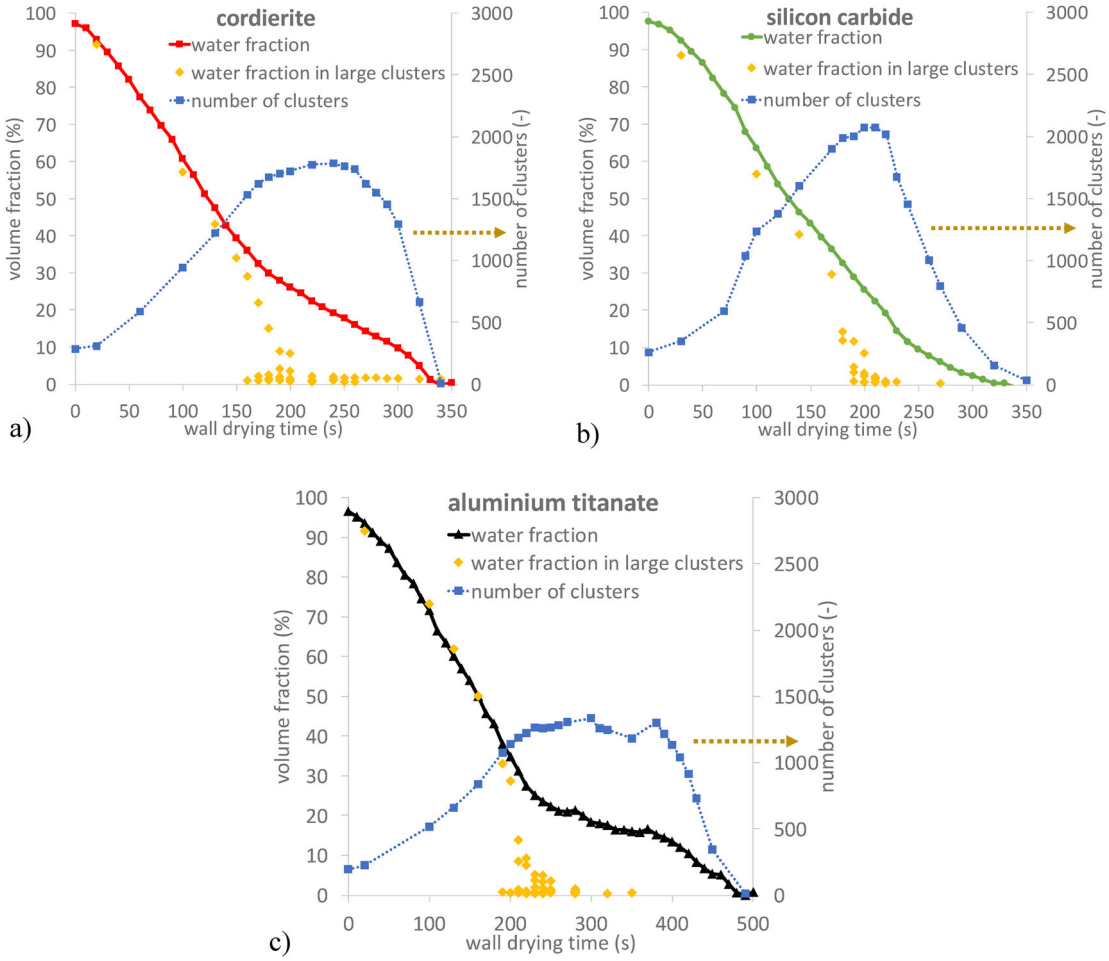


**Figure 11.** Temporal evolution of water clusters for (a) cordierite, (b) silicon carbide (SiC) and (c) aluminum titanate (AT). The volume of a large cluster is defined to be at least 150 times the volume of an average pore size. Each yellow diamond represents one large cluster. The number of clusters refers to the count of all clusters with a minimum volume equivalent to sphere with diameter of 4 μm (5 pixels).

shortly after the decomposition of the primary large cluster, Figure 11b. Thus, the 2nd CRP did not occur in the SiC sample, which indicates a more efficient wall drying during the 1st CRP compared to the other samples. We suggest that it is caused by the lower number of saturated large pore domains hidden behind narrow pore necks in SiC.

The very last drying period is generally characterized by the reduction of the water-air interface area as a consequence of clusters disappearing, and thus the observed drying rate should decrease (so-called *falling rate period*, FRP). Such a typical FRP behavior was observed for the SiC sample. However, the cordierite and AT structures showed an increase of water removal rate at the final stage of the drying process, see Figure 8 and Figure 11, more specifically wall drying times $t' > 300$ s for cordierite and $t' > 400$ s for AT. To understand this final increase of the reaction rate, the temperature evolution during the drying process must be analyzed. Figure 12 shows the temperature evolution measured in an independent drying experiment for a) cordierite, b) SiC and c) AT. Drying curves are shown as a temporal change of the mean gray value obtained from reconstructed 3 D images. At the onset of drying, after the heat guns had been moved into the sample position, the temperature quickly rose to approx. 40 °C and remained constant during the emptying of bulk water from the channels. The temperature subsequently decreased by 5–7 °C during the evaporation of the water film toward the end of the channel drying and the minimum was reached at the onset of the wall drying. The observed temperature drop can be explained by the reduction of thermal conductivity of the wetted system upon removal of water from the channels. Note that the thermal conductivity of air is approximately 20 times lower than that of water.

The drying curves from this independent experiment in presence of the thermocouple are compared to the measurement conducted without the

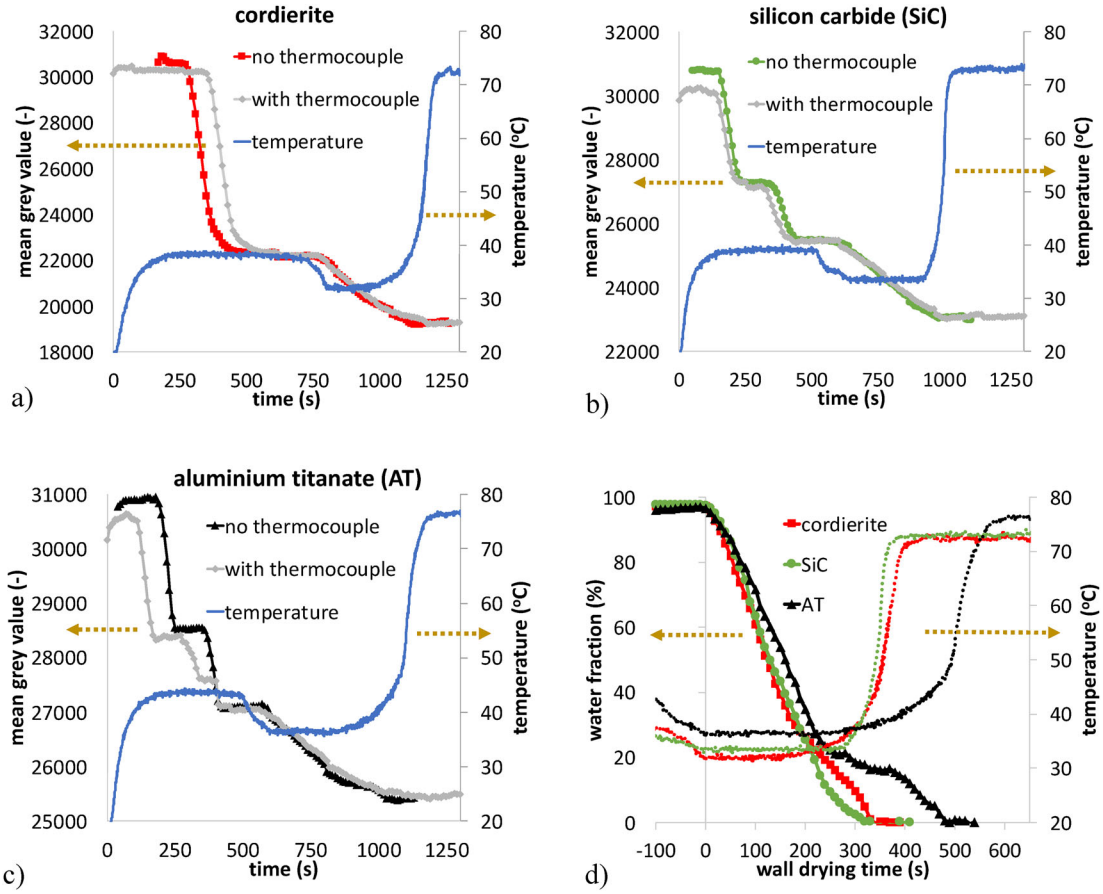


**Figure 12.** Evolution of temperature measured during drying of water from (a) cordierite, (b) silicon carbide and (c) aluminum titanate. Drying curves with and without the inserted thermocouple are compared. (d) Evolution of temperature and water fraction in all three samples. Wall drying time $t' = 0$ s indicates the onset of the wall drying.

thermocouple in Figure 12a–c. The duration of channel drying can vary due to weak capillary forces in the millimeter-sized channels, which leads to a different volume of soaked water. Therefore, drying curves measured with and without the thermocouple were normalized according to the onset of the wall drying with dominant capillary forces. The inserted thermocouple decreased the size of the dried channel, which can result in an additional step on the drying curve if the thermocouple is close to the field of view, see Figure 12c. As wall drying does not seem to be affected by the inserted thermocouple, the temperature evolution was plotted against the evaluated water fraction and compared for all samples, Figure 12d. During the 1st CRP of the wall drying, the sample temperature was constant for all three samples (cordierite 32 °C, SiC 33 °C and AT 36 °C), see Figure 12. The temperature variation between the substrates is caused by a different effective heat conductivity of the respective monolithic structures, which includes factors such as ceramic material, wall thickness, porosity and channel density. During the 2nd CRP in cordierite and AT, the sample temperature was slowly increasing, which accelerated in the last drying period. The SiC sample showed the steepest temperature increase during the FRP. Once all water was removed from the ceramic structure, the sample temperature increased quickly and reached a limit value: 72 °C for dry cordierite and SiC and 76 °C for dry AT. The rest of the heat provided by the heat guns was transferred to the surrounding air.

Knowing the exact evolution of temperature during the drying experiment, we can now better analyze the increased drying rate observed in the final period for cordierite and AT. Examination of the snapshots at the end of the 2nd CRP revealed the existence of isolated saturated pores located behind pore necks, Figure 13. The higher meniscus curvature at the pore necks decreases the equilibrium pressure of water vapor $p^*$ as dictated by the Kelvin equation:[59]

$$p^* = p_{\mathrm{sat}} \exp\left[-\frac{2\gamma V_{\mathrm{m}}}{r\mathrm{R}T}\right] \qquad (2)$$

where $p_{\mathrm{sat}}$ is the saturated vapor pressure over the flat interface, $\gamma$ is a surface tension, $V_{\mathrm{m}}$ denotes the molar volume, $r$ the pore radius, R is the universal gas

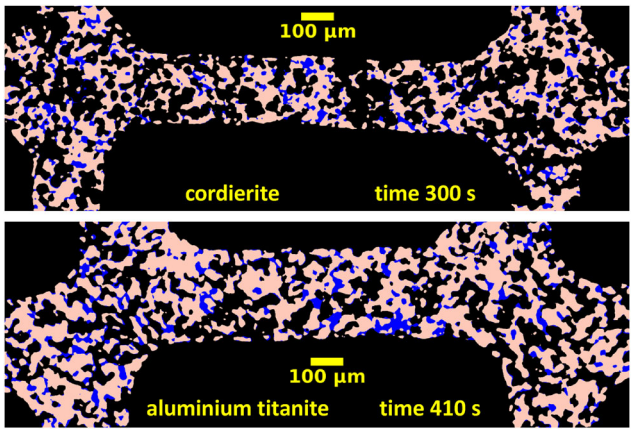


Figure 13. Snapshots of the water distribution inside the wall of cordierite and aluminum titanate at the end of the second constant rate period (2nd CRP). The wall drying time indicated in individual sub-figures shows the end of the 2nd CRP, which corresponds to the yellow color and triangle in Figure 8.

constant and $T$ the temperature. The driving force for the evaporation is expressed by the difference between the actual vapor pressure above the water meniscus $p_v$ and equilibrium vapor pressure $p^*$ corresponding to the temperature $T$ as showed by Hertz-Knudsen equation:[60]

$$r_v = (p^* - p_v)\alpha\sqrt{\frac{M}{2\pi RT}} \tag{3}$$

where $r_v$ is the evaporation rate, $\alpha$ the evaporation coefficient, $M$ the molar mass of water and R the universal gas constant. The 2nd CRP is characterized by a reduced drying rate due to diffusion-limited transport of vapor through the ceramic structure. Air inside the wall is thus saturated and smaller pores tend to dry later compared to the bigger ones, since their equilibrium vapor pressure $p^*$ is lower. The water meniscus at the entrance of the isolated water clusters is thus in equilibrium with the surrounding saturated air for the duration of the 2nd CRP. Hence, it can be assumed that the wall structure plays again an important role for the observed drying behavior.

The temperature rise during the last drying period of cordierite and AT increases saturation pressure of water vapor in the air according to the Antoine equation:

$$\log_{10} p_{sat} = A - \frac{B}{C + T} \tag{4}$$

where $T$ is temperature and A, B and C are constants. In addition, the higher temperature is beneficial for diffusive transport of the vapor according to:[61]

$$D_v = \frac{0.00143T^{1.75}}{p\sqrt{2/\left(\frac{1}{M_{H_2O}} + \frac{1}{M_{air}}\right)}\left(\sigma_{H_2O}^{\frac{1}{3}} + \sigma_{air}^{\frac{1}{3}}\right)^2} \tag{5}$$

where $p$ is total pressure, $M$ the molar mass and $\sigma$ the diffusion volume of the gas components. Therefore, the temperature rise in the last drying period accelerated water removal from the narrow pore necks, which in turn enabled opening and fast evaporation of residual water clusters entrapped behind them. This explains the higher drying rate observed in the very last drying period for cordierite and AT. As discussed previously, the SiC pore morphology with less restrictive pore necks did not exhibit this phenomenon.

## Conclusions

In this contribution, we applied time-resolved X-ray tomography, scanning electron microscopy and mercury intrusion porosimetry to investigate the dynamics of water drying in monolithic structures made of cordierite, silicon carbide (SiC) and aluminum titanate (AT). The distribution and re-distribution of water in porous ceramics was observed in three dimensions with a temporal resolution of 2 s. An image processing framework based on machine learning was developed to track pore emptying and filling in a large number of 3D scans (over hundred 3D scans per sample). Drying curves were constructed from the tomographic data to investigate drying in materials with a variety of structural properties. In monoliths with an asymmetric structure, bulk water is at first removed from the large channels followed by the small channels. A water film was formed in the rectangular corners and along the walls upon the retreat of the meniscus into the channel. Once the bulk water was completely removed from the channels, the surface and corner water film diminished, followed by drying of the porous walls. Drying of water from the monolith structures thus progresses in a hierarchical manner from millimeter-sized channels to micrometre-sized pores of the ceramic wall.

Different stages of wall drying were identified from the analyzed 4D images. Once air invaded the porous wall, the drying rate was constant (1st CRP) and approximately similar for all samples. A comparison of the water evolution near a wall-channel interface with water inside the ceramic wall revealed its flow toward the external surface. The drying rate on the wall-channel interface is the highest as it is not hindered by vapor diffusion through the wall pores. In addition, water removal from the ceramic wall resembled a cascade of events when a state with stable meniscus (stationary or relatively slowly receding) is followed by a rapid pore emptying (Haines jump). Interestingly, larger pores were emptied preferentially,

followed by the smaller ones in all three samples. Water is thus redistributed from the large to the small pores as well as from inside the ceramic wall to its external surface. The temporal evolution of clusters shows that the water inside the porous wall was initially interconnected to form one large cluster at the onset of drying. The size of this primary cluster decreased during drying, which was accompanied by menisci receding into the porous wall. The end of the 1st CRP was determined by the disintegration of the primary cluster, which led to a restriction of transport pathways to the external surface.

Cordierite and aluminum titanate exhibited a second constant drying period (2nd CRP) characterized by a slower drying rate. Larger water clusters continued to disintegrate, forming new water-air interfaces, which intensified drying inside the wall. However, the observed drying rate was constant during the 2nd CRP indicating that vapor transport through the ceramic wall was the rate-limiting process. Toward the end of the 2nd CRP, the number of clusters reached its maximum as the rate of newly generated clusters equals the rate of their disappearance due to drying. The end of the 2nd CRP was determined by the decline of the total number of clusters in cordierite and AT porous walls. The SiC sample showed a somewhat different behavior, since the maximum number of clusters was reached shortly after the decomposition of the primary water cluster. Thus, the 2nd CRP did not occur in SiC, suggesting more efficient wall drying during the 1st CRP compared to cordierite and AT.

The last drying period was characterized by the reduction of the air-water interface as a consequence of the clusters' disappearance. The decreasing rate in the last period was observed only for the SiC sample. On the contrary, cordierite and AT showed a temporary increase of the drying rate during the last drying period as opposed to the expectations in a system with reducing drying surface area. 3D images of cordierite and AT revealed the existence of saturated pores isolated behind narrow pore necks. In a diffusion limited regime, smaller pores tend to dry later than the bigger ones, since their equilibrium pressure over a curved interface is lower. The temperature rise in the last drying period accelerated water removal from the narrow pore necks, which in turn enabled opening and faster evaporation of residual water clusters entrapped behind them.

The developed approach to investigate the temporal and spatial distribution of water in the porous structure demonstrates that a direct observation of water drying in industrially relevant samples is experimentally achievable. The obtained information on the hierarchy of pore emptying, water redistribution and the size of water clusters provides a crucial link between the structural properties of dried materials and their drying rate. In this respect, time-resolved X-ray tomography represents an important tool, providing feedback for the design of porous materials with optimal drying performance. Furthermore, the achieved high spatial and temporal resolution of water removal from porous materials provides detailed experimental data for future developments of predictive mathematical models of the dynamic drying processes considering realistic 3D pore morphology.

## Acknowledgments

We acknowledge the Paul Scherrer Institut, Villigen, Switzerland for provision of synchrotron radiation beamtime at the TOMCAT beamline X02DA of the SLS.

## Disclosure statement

No potential conflict of interest was reported by the authors.

## Funding

VN acknowledges funding from the European Union's Horizon 2020 research and innovation programme under the Marie Skłodowska-Curie Grant Agreement No 701647. The work was further financially supported by the Czech Science Foundation (GA 19-22173S).

## Data availability statement

Raw and processed data obtained by time-resolved X-ray tomography are available at PSI Public Data Repository under doi.psi.ch/detail/10.16907/55e6177e-ed63-4615-839f-d5e202f49c68.

## References

[1] Van't Land, C. M. *Drying in the Process Industry*; **2012**. DOI: 10.1002/9781118105818.

[2] Kemp, I. C. Fundamentals of Energy Analysis of Dryers. In *Modern Drying Technology*; Wiley-VCH Verlag GmbH & Co. KGaA: Weinheim, Germany, **2012**; Vol. 4, pp 1–45. DOI: 10.1002/9783527631681.ch1.

[3] Kudra, T. Energy Aspects in Drying. *Dry. Technol.* **2004**, *22*, 917–932. DOI: 10.1081/DRT-120038572.

[4] Defraeye, T. Advanced Computational Modelling for Drying Processes—A Review. *Appl. Energy* **2014**, *131*, 323–344. DOI: 10.1016/j.apenergy.2014.06.027.

[5] Gascon, J.; Van Ommen, J. R.; Moulijn, J. A.; Kapteijn, F. Structuring Catalyst and Reactor - An Inviting Avenue to Process Intensification. *Catal. Sci. Technol.* **2015**, *5*, 807–817. DOI: 10.1039/C4CY01406E.

[6] Heck, R. M.; Farrauto, R. J.; Gulati, S. T. *Catalytic Air Pollution Control: Commercial Technology: Third Edition*. John Wiley: Hoboken, NJ, **2012**. DOI: 10.1002/9781118397749.

[7] Munnik, P.; De Jongh, P. E.; De Jong, K. P. Recent Developments in the Synthesis of Supported Catalysts. *Chem. Rev.* **2015**, *115*, 6687–6718. DOI: 10.1021/cr500486u.

[8] Nijhuis, T. A.; Beers, A. E. W.; Vergunst, T.; Hoek, I.; Kapteijn, F.; Moulijn, J. A. Preparation of Monolithic Catalysts. *Catal. Rev. Sci. Eng.* **2001**, *43*, 345–380. DOI: 10.1081/CR-120001807.

[9] Montebelli, A.; Visconti, C. G.; Groppi, G.; Tronconi, E.; Cristiani, C.; Ferreira, C.; Kohler, S. Methods for the Catalytic Activation of Metallic Structured Substrates. *Catal. Sci. Technol.* **2014**, *4*, 2846–2870. DOI: 10.1039/C4CY00179F.

[10] Kočí, P.; Isoz, M.; Plachá, M.; Arvajová, A.; Václavík, M.; Svoboda, M.; Price, E.; Novák, V.; Thompsett, D. 3D Reconstruction and Pore-Scale Modeling of Coated Catalytic Filters for Automotive Exhaust Gas After Treatment. *Catal. Today* **2019**, *320*, 165–174. DOI: 10.1016/j.cattod.2017.12.025.

[11] Novák, V.; Kočí, P.; Štěpánek, F.; Kubíček, M.; Marek, M.; Štěpánek, F.; Kubíček, M.; Marek, M. Simulated Preparation of Supported Porous Catalyst and Evaluation of Its Reaction-Transport Properties. *Comput. Chem. Eng.* **2011**, *35*, 964–972. DOI: 10.1016/j.compchemeng.2011.01.039.

[12] Lekhal, A.; Glasser, B. J.; Khinast, J. G. Impact of Drying on the Catalyst Profile in Supported Impregnation Catalysts. *Chem. Eng. Sci.* **2001**, *56*, 4473–4487. DOI: 10.1016/S0009-2509(01)00120-8.

[13] Scherer, G. W. Theory of Drying. *J. Am. Ceram. Soc.* **1990**, *73*, 3–14. DOI: 10.1111/j.1151-2916.1990.tb05082.x.

[14] Vu, H. T.; Tsotsas, E. Mass and Heat Transport Models for Analysis of the Drying Process in Porous Media: A Review and Numerical Implementation. *Int. J. Chem. Eng.* **2018**, *2018*, 1–13. DOI: 10.1155/2018/9456418.

[15] Kumar, N.; Arakeri, J. H. Investigation on the Effect of Temperature on Evaporative Characteristic Length of a Porous Medium. *Dry. Technol.* **2020**, *38*, 1194–1206. DOI: 10.1080/07373937.2019.1626877.

[16] Prat, M. On the Influence of Pore Shape, Contact Angle and Film Flows on Drying of Capillary Porous Media. *Int. J. Heat Mass Transf.* **2007**, *50*, 1455–1468. DOI: 10.1016/j.ijheatmasstransfer.2006.09.001.

[17] Lehmann, P.; Assouline, S.; Or, D. Characteristic Lengths Affecting Evaporative Drying of Porous Media. *Phys. Rev. E Stat. Nonlin. Soft Matter Phys.* **2008**, *77*, 056309. DOI: 10.1103/PhysRevE.77.056309.

[18] Zachariah, G. T.; Panda, D.; Surasani, V. K. Lattice Boltzmann Simulations for Invasion Patterns during Drying of Capillary Porous Media. *Chem. Eng. Sci.* **2019**, *196*, 310–323. DOI: 10.1016/j.ces.2018.11.003.

[19] Keita, E.; Koehler, S. A.; Faure, P.; Weitz, D. A.; Coussot, P. Drying Kinetics Driven by the Shape of the Air/Water Interface in a Capillary Channel. *Eur. Phys. J. E Soft Matter* **2016**, *39*, 1–10. DOI: 10.1140/epje/i2016-16023-8.

[20] Chauvet, F.; Duru, P.; Geoffroy, S.; Prat, M. Three Periods of Drying of a Single Square Capillary Tube. *Phys. Rev. Lett.* **2009**, *103*, 124502. DOI: 10.1103/PhysRevLett.103.124502.

[21] Ramskill, N. P.; Gladden, L. F.; York, A. P. E.; Sederman, A. J.; Mitchell, J.; Hardstone, K. A. Understanding the Operation and Preparation of Diesel Particulate Filters Using a Multi-Faceted Nuclear Magnetic Resonance Approach. *Catal. Today* **2013**, *216*, 104–110. DOI: 10.1016/j.cattod.2013.06.023.

[22] Koptyug, I. V. MRI of Mass Transport in Porous Media: Drying and Sorption Processes. *Prog. Nucl. Magn. Reson. Spectrosc.* **2012**, *65*, 1–65. DOI: 10.1016/j.pnmrs.2011.12.001.

[23] Hill-Casey, F.; Hotchkiss, T.; Hardstone, K. A.; Hitchcock, I.; Novak, V.; Schlepütz, C. M.; Meersmann, T.; Pavlovskaya, G. E.; Rigby, S. P. Hyperpolarised Xenon MRI and Time-Resolved X-Ray Computed Tomography Studies of Structure-Transport Relationships in Hierarchical Porous Media. *Chem. Eng. J.* **2021**, *405*, 126750. DOI: 10.1016/j.cej.2020.126750.

[24] Ohji, T.; Fukushima, M. Macro-Porous Ceramics: Processing and Properties. *Int. Mater. Rev.* **2012**, *57*, 115–131. DOI: 10.1179/1743280411Y.0000000006.

[25] Novák, V.; Dudák, M.; Kočí, P.; Marek, M. Understanding the Gas Transport in Porous Catalyst Layers by Using Digital Reconstruction Techniques. *Curr. Opin. Chem. Eng.* **2015**, *9*, 16–26. DOI: 10.1016/j.coche.2015.07.002.

[26] Govender, S.; Friedrich, H. Monoliths: A Review of the Basics, Preparation Methods and Their Relevance to Oxidation. *Catalysts* **2017**, *7*, 62. DOI: 10.3390/catal7020062.

[27] Perfect, E.; Cheng, C.-L.; Kang, M.; Bilheux, H. Z.; Lamanna, J. M.; Gragg, M. J.; Wright, D. M. Neutron Imaging of Hydrogen-Rich Fluids in Geomaterials and Engineered Porous Media: A Review. *Earth-Sci. Rev.* **2014**, *129*, 120–135. DOI: 10.1016/j.earscirev.2013.11.012.

[28] Fijał-Kirejczyk, I. M.; Milczarek, J. J.; Radebe, M. J.; de Beer, F. C.; Nothnagel, G.; Żołądek-Nowak, J. Neutron Radiography Applications in Studies of Drying of Capillary-Porous Systems. *Dry. Technol.* **2013**, *31*, 872–880. DOI: 10.1080/07373937.2013.779583.

[29] Li, J.; Qian, Z. Q. The Application of Image Acquisition and Analysis Techniques to the Field of Drying. *Food Eng. Rev.* **2017**, *9*, 13–35. DOI: 10.1007/s12393-016-9146-2.

[30] Strobl, M.; Manke, I.; Kardjilov, N.; Hilger, A.; Dawson, M.; Banhart, J. Advances in Neutron Radiography and Tomography. *J. Phys. D: Appl.*

*Phys.* **2009**, *42*, 243001. DOI: 10.1088/0022-3727/42/24/243001.

[31] Elique, A.; Eonard, L.; Crine, M.; Stepanek, F. 4 Use of X-Ray Tomography for Drying-Related Applications. In *Modern Drying Technology, Vol. 2: Experimental Techniques*, WILEY-VCH Verlag GmbH & Co. KGaA, Weinheim, **2009**; pp. 1–44.

[32] Haide, R.; Fest-Santini, S.; Santini, M. Use of X-Ray Micro-Computed Tomography for the Investigation of Drying Processes in Porous Media: A Review. *Dry. Technol.* **2021**, 1–14. DOI: 10.1080/07373937.2021.1876723.

[33] Kohout, M.; Grof, Z.; Stepánek, F. Pore-Scale Modelling and Tomographic Visualisation of Drying in Granular Media. *J. Colloid Interface Sci.* **2006**, *299*, 342–351. DOI: 10.1016/j.jcis.2006.01.074.

[34] Yang, F.; Griffa, M.; Bonnin, A.; Mokso, R.; Di Bella, C.; Münch, B.; Kaufmann, R.; Lura, P. Visualization of Water Drying in Porous Materials by X-Ray Phase Contrast Imaging. *J. Microsc.* **2015**, *261*, 88–104. DOI: 10.1111/jmi.12319.

[35] Shokri, N.; Sahimi, M. Structure of Drying Fronts in Three-Dimensional Porous Media. *Phys. Rev. E Stat. Nonlin. Soft Matter Phys.* **2012**, *85*, 066312. DOI: 10.1103/PhysRevE.85.066312.

[36] Davis, T. J.; Gao, D.; Gureyev, T. E.; Stevenson, A. W.; Wilkins, S. W. Phase-Contrast Imaging of Weakly Absorbing Materials Using Hard X-Rays. *Nature* **1995**, *373*, 595–598. DOI: 10.1038/373595a0.

[37] Wilkins, S. W.; Nesterets, Y. I.; Gureyev, T. E.; Mayo, S. C.; Pogany, A.; Stevenson, A. W. On the Evolution and Relative Merits of Hard X-Ray Phase-Contrast Imaging Methods. *Phil. Trans. R. Soc. A* **2014**, *372*, 20130021. DOI: 10.1098/rsta.2013.0021.

[38] Mokso, R.; Marone, F.; Irvine, S.; Nyvlt, M.; Schwyn, D.; Mader, K.; Taylor, G. K.; Krapp, H. G.; Skeren, M.; Stampanoni, M. Advantages of Phase Retrieval for Fast X-Ray Tomographic Microscopy. *J. Phys. D: Appl. Phys.* **2013**, *46*, 494004. DOI: 10.1088/0022-3727/46/49/494004.

[39] Villanova, J.; Daudin, R.; Lhuissier, P.; Jauffrès, D.; Lou, S.; Martin, C. L.; Labouré, S.; Tucoulou, R.; Martínez-Criado, G.; Salvo, L. Fast in Situ 3D Nanoimaging: A New Tool for Dynamic Characterization in Materials Science. *Mater. Today* **2017**, *20*, 354–359. DOI: 10.1016/j.mattod.2017.06.001.

[40] Marone, F.; Schlepütz, C. M.; Marti, S.; Fusseis, F.; Velásquez-Parra, A.; Griffa, M.; Jiménez-Martínez, J.; Dobson, K. J.; Stampanoni, M. Time Resolved in Situ X-Ray Tomographic Microscopy Unraveling Dynamic Processes in Geologic Systems. *Front. Earth Sci.* **2020**, *7*, 346. DOI: 10.3389/feart.2019.00346.

[41] Cybulski, A.; Moulijn, J. A. (Eds.). Structured Catalysts and Reactors (2nd ed.). CRC Press: Boca Raton, FL, 2005. DOI: 10.1201/9781420028003.

[42] Mokso, R.; Schlepütz, C. M.; Theidel, G.; Billich, H.; Schmid, E.; Celcer, T.; Mikuljan, G.; Sala, L.; Marone, F.; Schlumpf, N.; Stampanoni, M. GigaFRoST: The Gigabit Fast Readout System for Tomography. *J. Synchrotron Radiat.* **2017**, *24*, 1250–1259. DOI: 10.1107/S1600577517013522.

[43] Haberthür, D.; Hintermüller, C.; Marone, F.; Schittny, J. C.; Stampanoni, M. Radiation Dose Optimized Lateral Expansion of the Field of View in Synchrotron Radiation X-Ray Tomographic Microscopy. *J. Synchrotron. Radiat.* **2010**, *17*, 590–599. DOI: 10.1107/S0909049510019618.

[44] Paganin, D.; Mayo, S. C.; Gureyev, T. E.; Miller, P. R.; Wilkins, S. W. Simultaneous Phase and Amplitude Extraction from a Single Defocused Image of a Homogeneous Object. *J. Microsc.* **2002**, *206*, 33–40. DOI: 10.1046/j.1365-2818.2002.01010.x.

[45] Marone, F.; Stampanoni, M. Regridding Reconstruction Algorithm for Real-Time Tomographic Imaging. *J. Synchrotron. Radiat.* **2012**, *19*, 1029–1037. DOI: 10.1107/S0909049512032864.

[46] Parslow, A.; Cardona, A.; Bryson-Richardson, R. J. Sample Drift Correction following 4D Confocal Time-Lapse Imaging. *J. Vis. Exp.* **2014**, *86*, 1–4. DOI: 10.3791/51086.

[47] Thevenaz, P.; Ruttimann, U. E.; Unser, M. A Pyramid Approach to Subpixel Registration Based on Intensity. *IEEE Trans. Image Process.* **1998**, *7*, 27–41. DOI: 10.1109/83.650848.

[48] Rueden, C. T.; Schindelin, J.; Hiner, M. C.; DeZonia, B. E.; Walter, A. E.; Arena, E. T.; Eliceiri, K. W. ImageJ2: ImageJ for the Next Generation of Scientific Image Data. *BMC Bioinformatics.* **2017**, *18*, 529. DOI: 10.1186/s12859-017-1934-z.

[49] Schindelin, J.; Arganda-Carreras, I.; Frise, E.; Kaynig, V.; Longair, M.; Pietzsch, T.; Preibisch, S.; Rueden, C.; Saalfeld, S.; Schmid, B.; et al. Fiji: An Open-Source Platform for Biological-Image Analysis. *Nat Methods* **2012**, *9*, 676–682. DOI: 10.1038/nmeth.2019.

[50] Arganda-Carreras, I.; Kaynig, V.; Rueden, C.; Eliceiri, K. W.; Schindelin, J.; Cardona, A.; Seung, H. S. Trainable Weka Segmentation: A Machine Learning Tool for Microscopy Pixel Classification. *Bioinformatics* **2017**, *33*, 2424–2426. DOI: 10.1093/bioinformatics/btx180.

[51] Hildebrand, T.; Rüegsegger, P. A New Method for the Model-Independent Assessment of Thickness in Three-Dimensional Images. *J. Microsc.* **1997**, *185*, 67–75. DOI: 10.1046/j.1365-2818.1997.1340694.x.

[52] Bolte, S.; Cordelières, F. P. A Guided Tour into Subcellular Colocalization Analysis in Light Microscopy. *J. Microsc.* **2006**, *224*, 213–232. DOI: 10.1111/j.1365-2818.2006.01706.x.

[53] Rouquerol, J.; Baron, G.; Denoyel, R.; Giesche, H.; Groen, J.; Klobes, P.; Levitz, P.; Neimark, A. V.; Rigby, S.; Skudas, R.; et al. Liquid Intrusion and Alternative Methods for the Characterization of Macroporous Materials (IUPAC Technical Report). *Pure Appl. Chem.* **2011**, *84*, 107–136. DOI: 10.1351/PAC-REP-10-11-19.

[54] Washburn, E. W. The Dynamics of Capillary Flow. *Phys. Rev.* **1921**, *17*, 273–283. DOI: 10.1103/PhysRev.17.273.

[55] Blažek, M.; Žalud, M.; Kočí, P.; York, A.; Schlepütz, C. M.; Stampanoni, M.; Novák, V. Washcoating of Catalytic Particulate Filters Studied by Time-

Resolved X–Ray Tomography. *Chem. Eng. J.* **2021**, *409*, 128057. DOI: 10.1016/j.cej.2020.128057.

[56] Shokri, N.; Lehmann, P.; Or, D. Liquid-Phase Continuity and Solute Concentration Dynamics during Evaporation from Porous Media: Pore-Scale Processes near Vaporization Surface. *Phys. Rev. E Stat. Nonlin. Soft Matter Phys.* **2010**, *81*, 046308. DOI: 10.1103/PhysRevE.81.046308.

[57] Haines, W. B. Studies in the Physical Properties of Soil: V. The Hysteresis Effect in Capillary Properties, and the Modes of Moisture Distribution Associated Therewith. *J. Agric. Sci* **1930**, *20*, 97–116. DOI: 10.1017/S002185960008864X.

[58] Berg, S.; Ott, H.; Klapp, S. A.; Schwing, A.; Neiteler, R.; Brussee, N.; Makurat, A.; Leu, L.; Enzmann, F.; Schwarz, J.-O.; et al. Real-Time 3D Imaging of Haines Jumps in Porous Media Flow. *Proc. Natl. Acad. Sci. U S A.* **2013**, *110*, 3755–3759. DOI: 10.1073/pnas.1221373110.

[59] Thomson, W. LX. On the Equilibrium of Vapour at a Curved Surface of Liquid. *London, Edinburgh, Dublin Philos. Mag. J. Sci.* **1871**, *42*, 448–452. DOI: 10.1080/14786447108640606.

[60] Eames, I. W.; Marr, N. J.; Sabir, H. The Evaporation Coefficient of Water: A Review. *Int. J. Heat Mass Transf.* **1997**, *40*, 2963–2973. DOI: 10.1016/S0017-9310(96)00339-0.

[61] Fuller, E. N.; Schettler, P. D.; Giddings, J. C. A New Method for Prediction of Binary Gas-Phase Diffusion Coefficients. *Ind. Eng. Chem.* **1966**, *58*, 18–27. DOI: 10.1021/ie50677a007.